https://doi.org/10.26599/FRICT.2026.9441281

Research Article

# Streamline theory reveals bypass/trap effects in bio-inspired spine engagement dynamics

Zhonghuan Xiang[1], Xue Zhou[2], Peng Wei[1], Hui Cao[1], Hui Zhao[1], Wenqing Chen[1], Pengpeng Bai[1], Yonggang Meng[1], Liran Ma[1], Yu Tian[1,*]

[1.] *State Key Laboratory of Tribology in Advanced Equipment, School of Mechanical Engineering, Tsinghua University, Beijing 100084, China*

[2.] *School of Mechanical Engineering, Sichuan University, Chengdu 610065, China*

* Corresponding author. Yu Tian, E-mail: tianyu@mail.tsinghua.edu.cn

Received: August 13, 2025; Revised: May 11, 2026; Accepted: June 18, 2026





**Abstract**

This study introduces a streamline theory to reveal the micro-engagement dynamics of bio-inspired spines on rough surfaces. It first defines two key phenomena: the "bypass effect" and the "trap effect." Simulations demonstrate that the bypass effect reduces engagement effectiveness on convex asperities, while the trap effect significantly enhances engagement capacity on concave valleys. Experiments confirm these findings, revealing that the gain from the trap effect (252.2%) far outweighs the loss from the bypass effect (9.7%). Furthermore, analysis on fractal surfaces found that stable self-locking engagement occurs almost exclusively in concave regions (80%~90%) due to the trap effect. This research provides a theoretical foundation for bio-inspired gripping technology and functional surface design, with implications for future applications in effective grippers, robotics, and space exploration.

**Keywords**

Bio-inspired spines, streamline trajectory analysis, bypass/trap effects, frictional self-locking

## 1. Introduction

In nature, many organisms such as beetles[1–3], eagles[4,5], and bats exhibit remarkable abilities for robust adhesion and locomotion on various complex and rough surfaces. They achieve powerful attachment by engaging their spines with microscopic asperities (Fig. 1). By mimicking the efficient attachment capabilities of these creatures, humans have developed high-performance grippers[6–12] and climbing robots[13–24] that adapt to specific rough surface morphologies. These spiny climbing robots hold significant potential for applications in specialized terrains[25–34], particularly in microgravity environments for space exploration[35–37].

However, a comprehensive understanding of the micro-engagement dynamic mechanisms between spine tips and surface asperities remains limited, especially the underlying principles of efficient adhesion and self-locking. Existing studies have primarily focused on the static, two-dimensional characteristics of rough surfaces[38,39]. For instance, the sphere-to-sphere contact model proposed by Dai et al.[8,16] simplified asperities and spine tips into micro-hemispheres for force analysis. Asbeck et al.[40–42] first introduced the concepts of surface normal vector angle and engagement ratio, quantitatively characterizing the load-bearing capacity of a single engagement point by combining the two-dimensional surface profile geometry with the quantitative parameter of engagement ratio.

Our previous research on spine engagement theory had extended the analysis from two-dimensional curve morphology to three-dimensional rough surface morphology [43]. By analyzing the spatial coordinate distribution of the rough surface, the spatial engagement ratio was calculated, which in turn allowed for quantitative predictions regarding the spine's engagement capability and probability. Additionally, the influence of the spine's own spatial position characteristics, such as the pitch angle, on engagement capacity was taken into consideration, thereby explaining the phenomenon that biological spines in nature possess an optimal pitch angle.

Nevertheless, the aforementioned analyses were conducted on a point-by-point basis, applying the same engagement ratio analysis to every point on the rough surface. This approach overlooks the dynamic nature of the spine's actual movement and engagement process. Some theoretically calculated high-engagement regions may not be traversed by the spine, meaning that previous methods may have misjudged the actual engagement performance of the rough surface. For instance, two rough surfaces with similar static engagement ratios may exhibit vastly different actual engagement capabilities due to their distinct 3D topographies, which lead to completely different spine trajectories.

To address this limitation, this study proposes a streamline trajectory analysis method to reveal the micro-engagement dynamics of bio-inspired spines on complex rough surfaces. As shown in Fig. 1, two key phenomena were characterized and aligned with contact mechanics principles: the 'bypass effect' and the 'trap effect.' The bypass effect corresponds to contact instability on convex asperities, where the kinematic trajectory tends to deviate from the convex asperity, preventing the formation of stable contact (analogous to geometric exclusion). Conversely, the trap effect corresponds to geometric interlocking facilitated by a basin of attraction. Driven by the preload (e.g., gravity), the concave topography creates a potential energy gradient that actively draws the spine trajectory into the valleys, eventually stabilizing the spine tip into a state of stable equilibrium. Numerical simulations based on single Gaussian peaks, randomly distributed Gaussian surfaces, and random fractal surfaces consistently demonstrate that the bypass effect reduces engagement effectiveness on convex asperities, while the trap effect significantly enhances engagement capacity on concave valleys. Experiments using P36, P60, and P600 sandpapers confirm these theoretical findings and reveal that the gain from the trap effect (252.2%) far outweighs the loss from the bypass effect (9.7%). Furthermore, studies on fractal surfaces, utilizing the sectional and Hessian matrix methods for convexity analysis, reveal that self-locking engagement occurs predominantly in concave regions, establishing the dominant role of valleys in efficient engagement. This research provides a new theoretical foundation for bio-inspired gripping technology and functional surface design, with significant implications for future applications in grippers, robotics, and aerospace exploration.

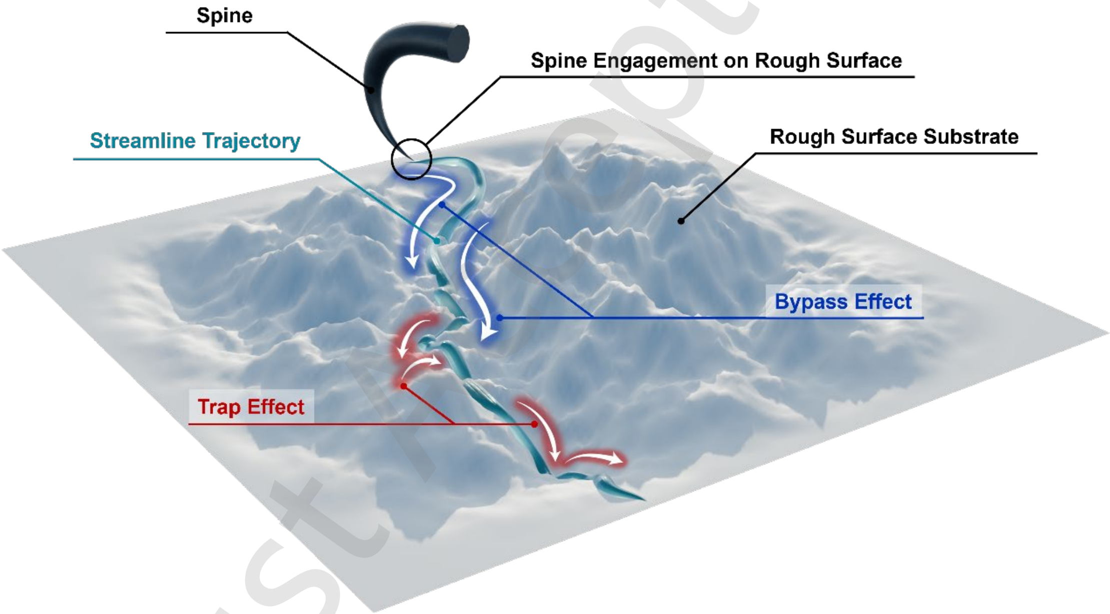


**Fig. 1 Streamline trajectory in spine-asperities engagement and bypass/trap effect.**

## 2. Theoretical framework and methodologies

### 2.1 Force analysis and engagement ratio $\kappa$

The contact engagement process of a spine on a rough surface can be analyzed by examining the forces exerted on it at a single asperity. As illustrated in Fig. 2A, the force interaction on the spine tip over a single convex Gaussian asperity is investigated. For simplification, the spine is modeled as a point contact, thereby neglecting its finite shape and orientation. This assumption is justified in macro-rough engagement scenarios (typical of effective engagement, such as the P36 and P60 cases examined later), where the spine tip radius ($R_{tip} \approx 25$ μm) is orders of magnitude smaller than the characteristic macro-scale asperities of the rough surface. Furthermore, considering Hertzian contact mechanics, the actual effective contact area is substantially smaller than the tip radius itself.

While previous studies have highlighted the influence of the spine's pitch angle and tip radius [8,41], specifically noting that sharper spines maximize engagement potential by accessing finer surface details. This study adopts the point contact model to represent the kinematic limit. This approach allows us to focus solely on the force behavior and dynamic trajectory at the contact point, isolating the intrinsic bypass and trap effects from the geometric filtering caused by a finite tip radius (a factor that becomes dominant only when the surface roughness decreases to the scale of the tip, as discussed in the P600 boundary case).

As depicted in Fig. 2A, the spine is subjected to a downward gravitational force $W$ (or other preloading forces) and a driving force $F$ acting in the positive x-direction. Their resultant force is $R$. Engagement occurs on the rising slope of the convex Gaussian asperity. The tangent plane at the engagement point is also shown in the figure. The projection of the driving force $F$ onto the tangent plane is $T_x$, and the projection of the gravitational force $W$ onto the tangent plane is $T_W$. Their resultant force is $T$. Assuming the Gaussian asperity is undeformable, the slip direction of the spine tip is constrained to the direction of the tangent plane at the engagement point. Therefore, the resultant force $T$ along the tangent plane represents the force that drives the spine tip to slide within the tangent plane at the engagement point, essentially representing the force that breaks the engaged state. The direction of force $T$ indicates the slip direction of the spine tip after the engaged state is broken. It is important to note that previous research typically focused on engagement-slipping phenomena on two-dimensional curves, where the slipping direction is fixed. In a three-dimensional space, however, the slipping direction is also a quantity related to the critical slipping state. This is because variations in the magnitude of the external force $F$ at the moment of slipping can alter the direction of the resultant force $R$.

To quantitatively describe the load-bearing capacity of an engagement point, the engagement ratio $(\kappa)$ is defined as $\kappa = F_c/W$, where $F_c$ is the maximum external driving force that can be applied before slipping occurs. This parameter was first proposed by Asbeck et al.[41] and has since been widely applied in static 2D spine engagement analysis. Building on this work, the current study extends the concept of a static 2D κ to a dynamic 3D engagement ratio for a given engagement point. To quantitatively calculate this, the direction of the driving force $F$ is defined as $\boldsymbol{u_x} = [1,0,0]$, and the gravitational force $W$ as $u_z^-$=[0,0,-1]. The normalized surface normal vector at the contact point is given by $\boldsymbol{n} = \left[n_x, n_y, n_z\right] = \frac{1}{\|\boldsymbol{n_0}\|}\left[\frac{\partial z}{\partial x}, \frac{\partial z}{\partial y}, -1\right]$.

The total resultant force $\boldsymbol{R} = F\boldsymbol{u_x} + W\boldsymbol{u_z^-}$ is decomposed into its normal magnitude $N = \boldsymbol{R} \cdot \boldsymbol{n}$ and tangential vector $\boldsymbol{T} = \boldsymbol{R} - (\boldsymbol{R} \cdot \boldsymbol{n})\boldsymbol{n}$. The critical condition for the spine tip to maintain static engagement is governed by the Coulomb friction law:

$$\|\boldsymbol{T}\| = \mu_s N \tag{1}$$

where $\mu_s$ is the static friction coefficient. By substituting the force components into Eq. (1), squaring both sides to eliminate the vector norms, and rearranging the terms with respect to the engagement ratio $\kappa$, the critical condition simplifies to a quadratic equation:

$$A\kappa^2 + B\kappa + C = 0 \tag{2}$$

where the coefficients are derived as:

$$\begin{cases} A = \|\boldsymbol{T}_{\boldsymbol{x}}^{*}\|^2 - \mu_s^2 n_x^2 \\ B = 2(\boldsymbol{T}_{\boldsymbol{x}}^{*} \cdot \boldsymbol{T}_{\boldsymbol{W}}^{*} + \mu_s^2 n_x n_z) \\ C = \|\boldsymbol{T}_{\boldsymbol{W}}^{*}\|^2 - \mu_s^2 n_z^2 \end{cases} \tag{3}$$

Here, $\boldsymbol{T}_{\boldsymbol{x}}^{*} = \boldsymbol{u}_{\boldsymbol{x}} - n_x \boldsymbol{n}$ and $\boldsymbol{T}_{\boldsymbol{W}}^{*} = \boldsymbol{u}_{\boldsymbol{z}}^{-} + n_z \boldsymbol{n}$ represent the non-dimensionalized tangential components of the driving and gravitational forces, respectively. The discriminant of the quadratic Eq. (2) is defined as $\Delta = B^2 - 4AC$. Solving Eq. (2) allows for the determination of the engagement ratio $\kappa$ for a given engagement point.

Fig. 2B illustrates the distribution of the engagement ratio on convex and concave Gaussian asperities, with specific $\kappa$ values indicated by the color bar. Blue represents smaller $\kappa$ values, while red indicates larger $\kappa$ values; both colors collectively denote the engagement region. Deep red signifies the self-locking region, where $\kappa$ is infinitely large, implying that once engagement occurs in this area, no magnitude of force $F$ can break the engaged state. Conversely, colorless regions represent the slip region, where $\kappa$ does not exist. In these areas, the spine tip slides off under gravity and cannot maintain a stable position. The discriminant flowchart for the self-locking region, slip region, and engagement region, corresponding to equations (2) and (3), is provided in Fig. 2C.

First, when $A < 0$ (or $A = B = 0$ and $C < 0$), it is inferred that for sufficiently large $\kappa$, $A\kappa^2 + B\kappa + C < 0$, which implies $\|\boldsymbol{T}\| < \mu_s N$. This suggests that when force $F$ is sufficiently large, it will not cause slipping. If, in addition, force $F$ is directed inward towards the surface (non-detachment condition), the engagement point is classified within the self-locking region.

If the self-locking condition is not met, and either $A = B = 0$ or the discriminant of the quadratic equation $\Delta < 0$, then no real roots exist for $\kappa$. This indicates that no engagement-slip transition process occurs at the spine tip's current location. Since the self-locking region has been excluded, this scenario must correspond to the slip region. In such cases, the spine tip cannot remain at that point and will slide down under the influence of gravity, following the direction of the gravity component in the tangent plane, until it enters an engagement region (or self-locking region).

When the discriminant of the quadratic equation $\Delta > 0$, positive real roots for $\kappa$ exist, provided that the force $N$ points inward towards the surface (non-detachment condition). This implies that a critical positive value of $\kappa$ exists, such that engagement occurs when $F < \kappa W$, and slipping occurs when $F > \kappa W$. The calculated $\kappa$ then characterizes the load-bearing capacity of that point. If two positive $\kappa$ values are calculated, the larger value is selected. This is because the smaller value represents the critical condition for the engagement point not to slip under gravity $W$, whereas the larger $\kappa$ signifies the critical condition for the engagement point not to slip under the external driving force $F$.

The resulting $\kappa$ distribution, calculated as described above, is plotted in Fig. 2B. As evident from the figure, for a convex Gaussian asperity, the engagement and self-locking regions with larger $\kappa$ values are primarily concentrated on the rising slope of the convex asperity, while the opposite descending slope constitutes the slip region.

Conversely, for a concave Gaussian valley, the engagement and self-locking regions with larger $\kappa$ values are mainly located on the rising slope where the hollow begins to ascend, whereas the initial descending slope of the hollow is the slip region. The patterns observed in both cases are similar. Due to symmetry, it is also observed that for identical Gaussian distribution parameters, the $\kappa$ distributions for convex Gaussian peaks and concave Gaussian valleys are symmetrical, and their self-locking areas are identical. Consequently, subsequent differences in the streamline trajectories analysis of engagement are not attributable to variations in the engagement ratio $\kappa$ distribution.

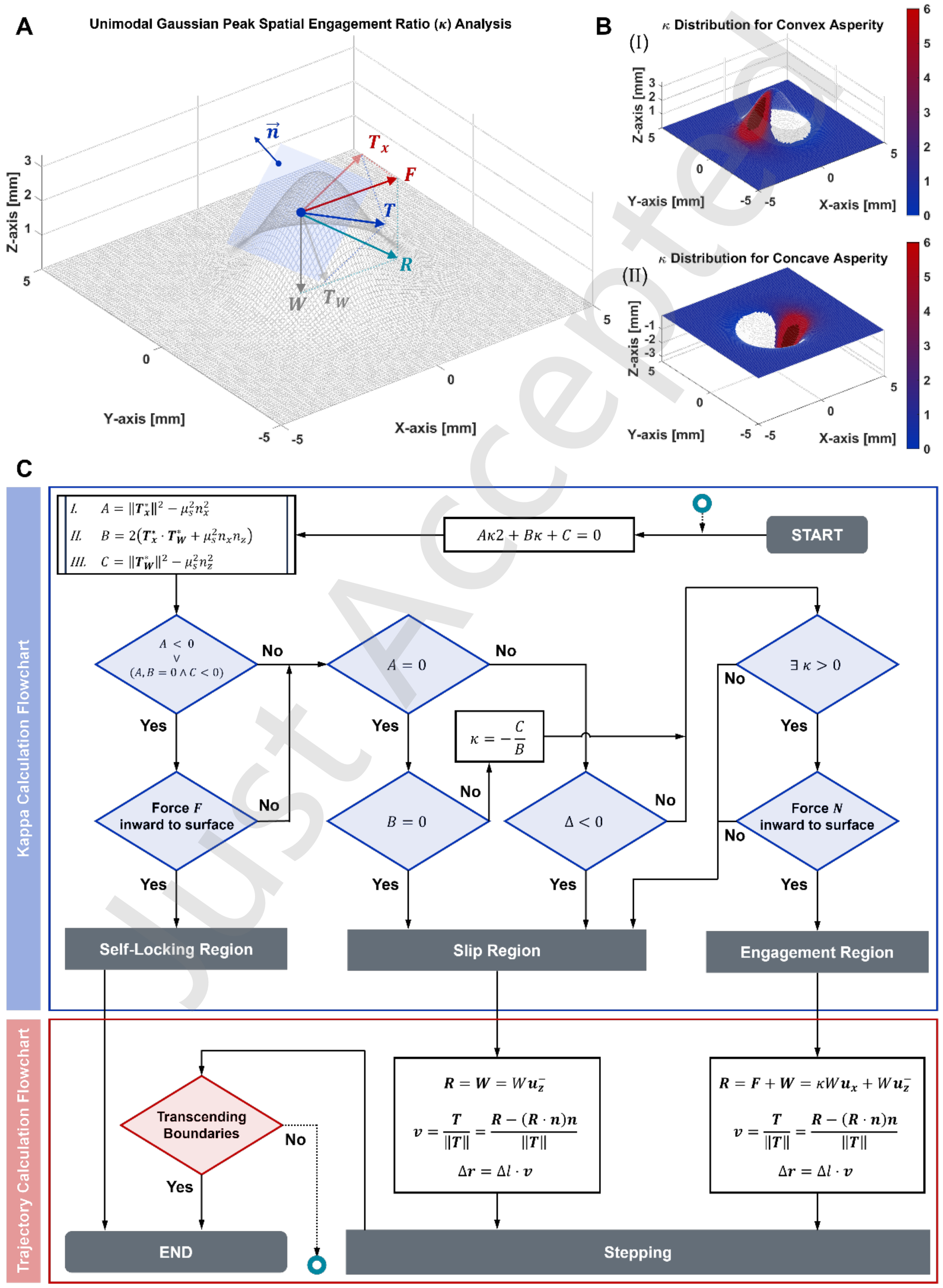



**Fig. 2. Engagement ratio $\kappa$ distribution and trajectory calculation.** (A) Force analysis of a spine engaging with a single Gaussian asperity. (B) Distribution of the engagement ratio ($\kappa$) on a single convex Gaussian peak and a concave Gaussian valley. (C) Flowchart for calculating the

engagement ratio ($\kappa$) and the engagement streamline trajectory.

### 2.2 Streamline trajectory generation algorithm

Based on the calculated three-dimensional distribution of the engagement ratio ($\kappa$), the subsequent slip direction of the spine tip after engagement failure at a specific contact point can be further derived. This allows for the step-by-step computation of an engagement streamline. Assuming the engagement-detachment-re-engagement process is quasistatic, without considering complexities like stick-slip phenomena or acceleration, a quasistatic engagement trajectory streamline of the spine tip on the rough surface can be calculated.

In practical scenarios, if the spine's motion is not excessively fast, allowing the spine tip sufficient time to adjust its engagement state at a given point, its actual trajectory can be considered quasistatic. Overly fast spine motion can cause the spine tip to "jump" on the rough surface (similar to stick-slip behavior), which is detrimental to spine engagement.

The applicability boundary of this quasistatic approximation can be estimated by a dimensionless engagement inertia number, $I_{\mathrm{e}}=\frac{m_{\mathrm{eff}}\, v^2}{F_{\mathrm{p}}\, L_{\mathrm{c}}}$, where $m_{\mathrm{eff}}$ is the effective moving mass of the spine assembly, $v$ is the tangential engagement velocity, $F_{\mathrm{p}}$ is the normal preload, and $L_{\mathrm{c}}$ is the characteristic asperity length scale. When $I_{\mathrm{e}} \ll 1$, the kinetic energy over one surface feature is much smaller than the preload work required to reorient the spine tip, so the tip can settle onto the local surface before the next engagement-slip event. When $I_{\mathrm{e}}$ approaches or exceeds unity, inertial jumping and stick-slip motion may cause the spine to skip over concave valleys or detach from convex asperities, so the present model should be regarded as qualitatively indicative rather than quantitatively predictive.

The flowchart for calculating the quasistatic engagement streamline trajectory is shown in Fig. 2C. For a specific engagement point, it is assumed that the applied driving force $F$ slowly increases from zero until it reaches the engagement limit $\kappa W$ for that point, at which stage the engagement state breaks. At this critical point, the resultant force is $\boldsymbol{R} = \boldsymbol{F} + \boldsymbol{W} = \kappa W \boldsymbol{u_x} + W \boldsymbol{u_z^-}$. The spine tip then steps in the direction of detachment. The normalized slip direction vector is calculated as $\boldsymbol{v} = \frac{\boldsymbol{T}}{\|\boldsymbol{T}\|}$. After stepping a length $\Delta l$, the displacement vector is simply $\boldsymbol{\Delta r} = \Delta l \cdot \boldsymbol{v}$.

The step size $\Delta l$ determines the resolution of the trajectory. To ensure numerical convergence and accuracy, $\Delta l$ is selected to be sufficiently small relative to the characteristic scale of the surface asperities (e.g., $\Delta l \approx 0.01\sigma$ for Gaussian surfaces). A sensitivity analysis confirmed that further reducing the step size yields negligible deviations in the calculated trajectory, ensuring that the discrete steps accurately approximate the continuous sliding process on the curved surface.

Assuming the initial landing position vector is $\boldsymbol{A_0} = \boldsymbol{B_0} = (x_0, y_0, z_0)$, where $z_0 = f(x_0, y_0)$ is the rough surface function, the iterative formula for the trajectory can be expressed as:

$$\begin{cases} \boldsymbol{A_{k+1}} = \boldsymbol{A_k} + \Delta \boldsymbol{r_k} = \boldsymbol{A_k} + \Delta l \cdot \boldsymbol{v_k} \\ \boldsymbol{B_{k+1}} = \left(A_{k+1,x}, A_{k+1,y}, f\left(A_{k+1,x}, A_{k+1,y}\right)\right) \end{cases} \tag{4}$$

The final engagement streamline trajectory is composed of the discrete stepped points $\{\boldsymbol{B_0}, \boldsymbol{B_1}, \dots, \boldsymbol{B_n}\}$. The process of transitioning from $\{\boldsymbol{A_0}, \boldsymbol{A_1}, \dots, \boldsymbol{A_n}\}$ to $\{\boldsymbol{B_0}, \boldsymbol{B_1}, \dots, \boldsymbol{B_n}\}$ follows the principle of gravitational reorientation under quasi-static conditions, which ensures that the engagement streamline always remains on the surface. This process is repeated until a termination condition is met: (1) the spine tip enters the self-locking region, or (2) the spine tip moves beyond the calculated surface range.

Notably, if the spine tip falls into the slip region, it cannot bear any driving force $F$ and will slide along the rough surface in the direction of the gravity component. In this specific case, the resultant force $\boldsymbol{R}$ is modified to $\boldsymbol{R} = \boldsymbol{W} = W\boldsymbol{u_z^-}$, while the rest of the calculation logic remains unchanged.

Overall, the quasistatic engagement streamline trajectory is calculated through a cyclic process involving force equilibrium, tangential direction calculation, local linear movement, and surface correction. The core physical process entails: first, calculating the engagement ratio $\kappa$ at a given point and determining its region type. Subsequently, the tangential slip direction $\boldsymbol{v}$ is calculated, and a step of $\Delta l$ is taken. Finally, surface correction is applied to project the series of points $\{\boldsymbol{A_0}, \boldsymbol{A_1}, \dots, \boldsymbol{A_n}\}$ to $\{\boldsymbol{B_0}, \boldsymbol{B_1}, \dots, \boldsymbol{B_n}\}$, thereby ensuring the trajectory remains on the surface.

## 3. Results and discussion

### 3.1 "Bypass effect" and "trap effect" on single gaussian peaks

#### 3.1.1 Trajectory visualizations

Fig. 3 displays multi-angle views of simulated engagement streamline trajectories within the region $-5 < x < 5, -5 < y < 5$. These simulations were performed on a single-peak convex Gaussian peak and a concave Gaussian valley, using parameters $\mu_x = \mu_y = 0, \sigma_x = \sigma_y = 1.5$, and $k = 10\pi$. Five initial starting points were selected at $x = -3$ with $y = -4, -3, -2, -1, -0.5$. The trajectories were generated using the previously discussed engagement streamline algorithm under the influence of an external driving force $F$ in the positive x-direction and gravity $W$.

Fig. 3 includes overall views of the five trajectories from the rear (Fig. 3A for convex and Fig. 3D for concave), along with observational views from the front-side, rear-side, and top perspectives (Fig. 3B for convex and Fig. 3C for concave). The starting point of the trajectory is denoted by an open circle, and the end point is indicated by a cross mark.

For the single-peak convex Gaussian peak (Fig. 3A-B), all trajectories demonstrated a tendency to "bypass" the protruding asperity due to gravity. Trajectories starting closer to the asperity's center achieved greater climbing heights. However, they invariably slipped after climbing a certain distance and subsequently "bypassed" the single-peak convex Gaussian asperity. This indicates that in spine-asperity engagement, the spine's engagement trajectory tends to avoid convex asperities, a phenomenon termed the "bypass effect."

Similarly, for the single-peak concave Gaussian valley (Fig. 3C-D), the trajectories consistently exhibited a tendency to "fall into" the valley, also due to gravity. Trajectories originating closer to the valley's center became entrapped earlier. In contrast, trajectories further from the center entered the valley later, with only the curve farthest from the center ($x = -3, y = -4$) completely avoiding entrapment. All trajectories that fell into the valley (initial $y$ values of $-3, -2, -1, -0.5$) ultimately reached a self-locking state, as their termination condition was entry into the self-locking region, not exceeding the computational boundary. This phenomenon, where the spine's movement trajectory becomes entrapped in concave valleys when approaching rough surface valleys, is referred to as the "trap effect."

The existence of the bypass and trap effects leads to significant differences in engagement streamline trajectories between convex and concave rough surfaces, even for identical relative starting points. The bypass effect causes trajectories to circumvent the rising slope of convex asperities. Crucially, these bypassed regions often correspond to engagement areas (or self-locking regions) with higher $\kappa$ values. Consequently, the presence of the bypass effect suggests that spine engagement on convex asperities becomes more challenging than what static $\kappa$ predictions alone might suggest. Conversely, the trap effect causes engagement streamline trajectories to be drawn into concave valleys, even if their starting points are some distance from the self-locking region. This leads them to reach engagement areas (or self-locking regions) with larger $\kappa$ values than they would by progressing straight. Therefore, the presence of the trap effect implies that spine engagement on concave valleys becomes easier and more efficient compared to predictions based purely on static $\kappa$.

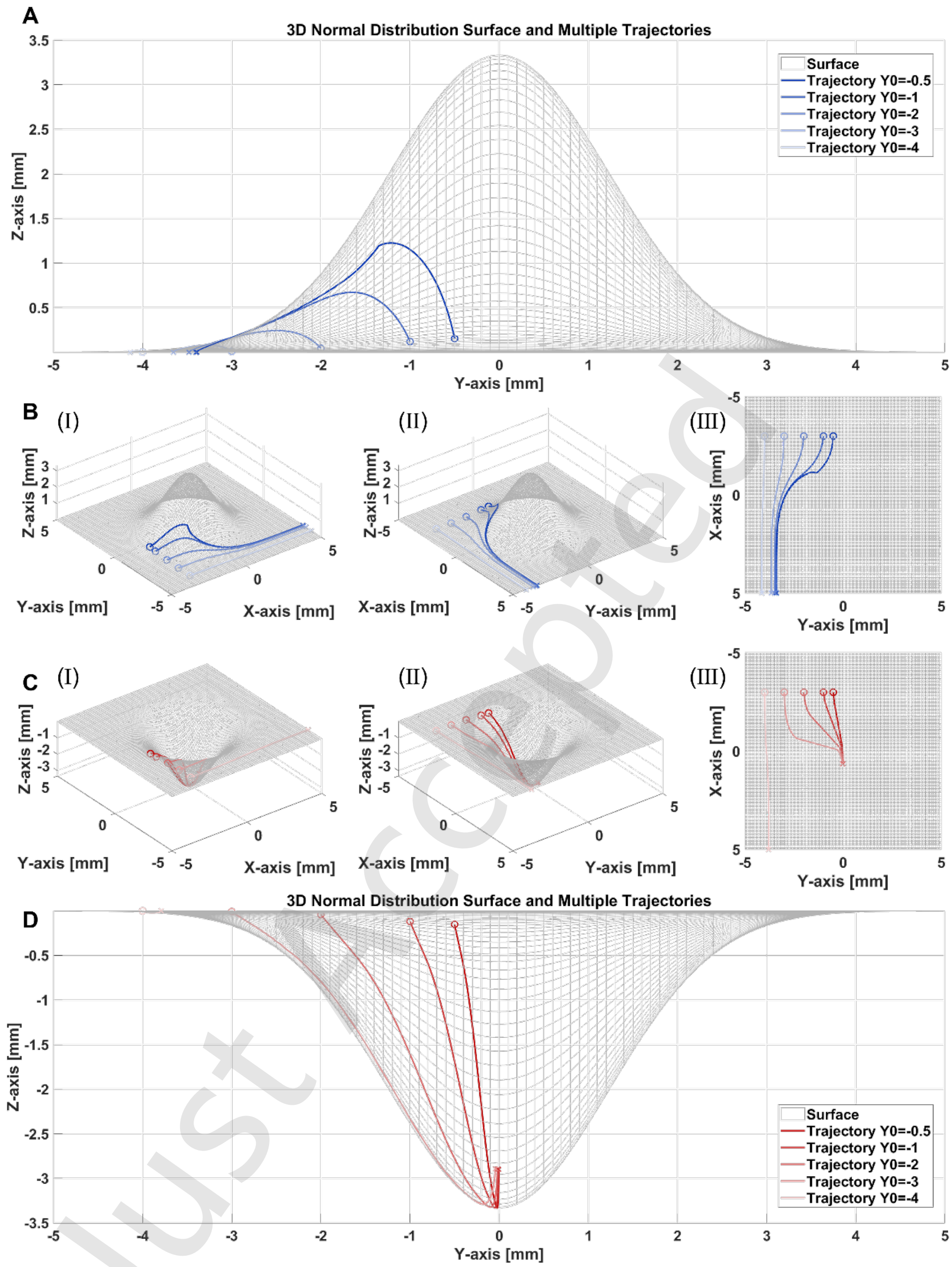




**Fig. 3. Simulated engagement streamline trajectories on single-peak convex and concave Gaussian asperities.** (A) Overall rear view of engagement streamline trajectories for the single-peak convex Gaussian peak. (B) Front-side, rear-side, and top observational views of engagement streamline trajectories for the single-peak convex Gaussian peak. (C) Front-side, rear-side, and top observational views of engagement streamline trajectories for the single-peak concave Gaussian valley. (D) Overall rear view of the engagement streamline trajectories for the single-peak concave Gaussian valley.

### 3.1.2 Quantitative analysis of $\kappa$

Fig. 3 presents the differences in streamline engagement trajectories calculated for different starting points on single convex and concave Gaussian peaks. To further investigate the influence of these differences on engagement performance, Fig. 4 shows the corresponding $\kappa$ variation curves along the five trajectories mentioned above. To more clearly describe the effects of the bypass and trap phenomena, the concepts of ideal and streamline trajectories are defined. The trajectories calculated by the algorithm considering the combined effects of gravitational force $W$ and external driving force $F$ are referred to as streamline trajectories. Conversely, trajectories formed by the spine tip moving along the direction of the external force $F$ on the curved surface, without considering the bypass and trap effects, are termed ideal trajectories. The y-value of an ideal trajectory remains constant, always fixed at its initial y-value.

Fig. 4A plots the $\kappa$ value curves for each of the five streamline trajectories on the single convex Gaussian peak, compared to their corresponding ideal trajectories with the same starting points. In this figure, a $\kappa$ value of infinity, which exceeds the plotting range when a self-locking state is reached, is indicated by an upward-pointing triangular arrow. The following observations were made: (1) The engagement ratio $\kappa$ increases on the rising slope of the first half of the single convex Gaussian peak, where its value is in a larger range, and sharply decreases on the descending slope of the second half. This aligns with the analysis in Fig. 2B. (2) The peak $\kappa$ value of the ideal trajectory is consistently greater than that of the streamline trajectory. The closer the trajectory is to the center, the greater this difference becomes. For example, as shown in Fig. 4A(I), where $y_0 = -0.5$ and is closest to the center, the ideal trajectory reaches a self-locking state on the rising slope of the Gaussian peak, whereas the $\kappa$ of the streamline trajectory only shows some fluctuations. In contrast, as shown in Fig. 4A(V), where $y_0 = -4$ and is farthest from the center, the $\kappa$ curves of the ideal and streamline trajectories are very close, with the ideal trajectory's maximum $\kappa$ being slightly larger. This indicates that the bypass effect is more pronounced closer to the center, as its presence leads to a greater loss in maximum $\kappa$. (3) The closer the starting point is to the center, the larger the $\kappa$ value is for both the ideal and streamline trajectories. This is because being closer to the center means being closer to the engagement region (or self-locking region) with larger $\kappa$ values, which is also consistent with the analysis in Fig. 2B. Fig. 4A(VI) presents the $\kappa$ curves for all five trajectories, providing a more intuitive view of this conclusion.

Similarly, Fig. 4D plots the $\kappa$ value curves for each of the five streamline trajectories on the single concave Gaussian peak, compared to their corresponding ideal trajectories with the same starting points. It can be seen from the figure that: (1) $\kappa$ rapidly increases on the rising slope of the second half of the concave Gaussian peak, while it remains approximately zero on the descending slope of the first half. This is consistent with the analysis in Fig. 2B. (2) The peak $\kappa$ value of the ideal trajectory is consistently smaller than that of the streamline trajectory. In regions closer to the center (e.g., Fig. 4D(I)), both enter a self-locking state, with little difference. When slightly farther from the center (e.g., Fig. 4D(II-IV)), the ideal trajectory does not self-lock, but the streamline trajectory still enters self-locking due to the trap effect. When very far from the center (e.g., Fig. 4D(V)), neither the ideal nor the streamline trajectory self-locks, and the difference is again small. (3) The closer the starting point is to the center, the larger the $\kappa$ is for both the ideal and streamline trajectories, similar to the previous analysis. Fig. 4D(VI) plots the $\kappa$ curves for all five trajectories together, providing a more intuitive view of this conclusion.

In summary, the bypass effect causes the $\kappa$ of a streamline trajectory to be smaller than that of an ideal trajectory, with this difference being more significant closer to the center. Conversely, the trap effect causes the $\kappa$ of a streamline trajectory to be greater than that of an ideal trajectory, with the difference becoming less significant only at very large distances from the center. To quantitatively characterize these two influences, the corresponding curves of the initial starting point y-value versus the maximum $\kappa$ value on the streamline trajectory were plotted for the single convex Gaussian peak (Fig. 4B) and the concave Gaussian valley (Fig. 4C). In these figures, the self-locking regions are indicated, including the ranges where the ideal trajectory enters the ideal self-locking region (same as Fig. 2B) and the starting point ranges where the streamline trajectory enters self-locking considering the bypass and trap effects. It can be observed that, due to the bypass effect, the streamline self-locking region for the single convex Gaussian peak is slightly smaller than the ideal self-locking region (83.3%). However, for the single concave Gaussian valley, the streamline self-locking region is significantly larger than the ideal self-locking region (566.7%). This suggests that the trap effect has a far more significant impact on the load-bearing capacity of the engagement. Specifically, the concave part of a rough surface makes it much easier for a spine to enter a highly efficient engagement state (or self-locking engagement state) than what would be predicted by a simple $\kappa$ calculation.

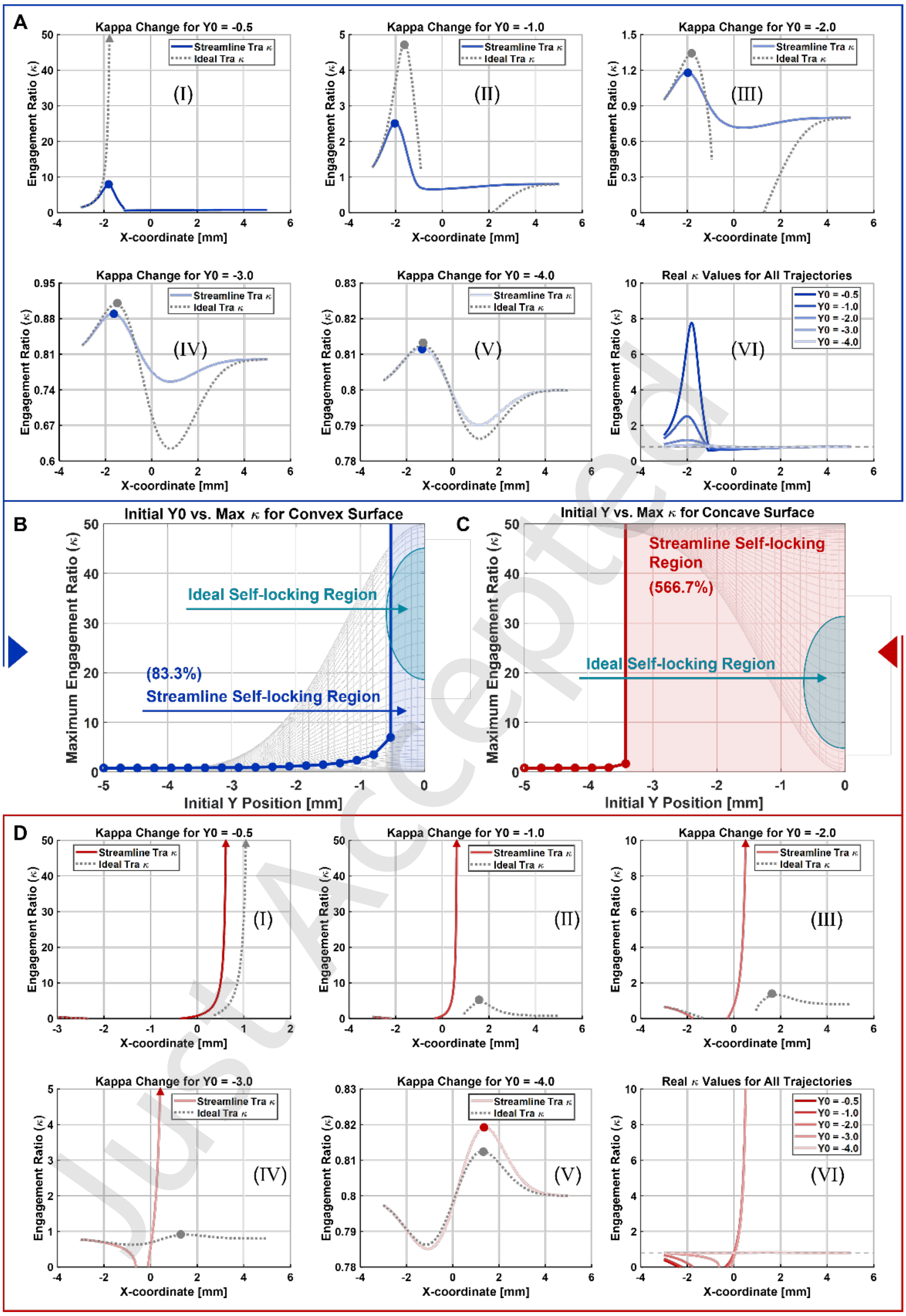


**Fig. 4. κ distributions of streamline trajectories on single Gaussian peaks.** (A) Comparison of κ distributions for streamline and ideal trajectories on a single convex Gaussian peak. (B) Comparison of streamline and ideal self-locking regions on a single convex Gaussian peak under the influence of the bypass effect. (C) Comparison of streamline and ideal self-locking regions on a single concave Gaussian valley under the influence of the trap effect. (D) Comparison of κ distributions for streamline and ideal trajectories on a single concave Gaussian valley.

### 3.2 Randomly distributed gaussian rough surfaces

Based on the analysis of single Gaussian peaks, the bypass and trap effects on spine engagement with rough surfaces were fundamentally explained. However, real surfaces are often composed of numerous asperities. Therefore, to better simulate a real surface, a random rough surface composed of $N = 100$ random Gaussian peaks was generated in the range of $-10 < x < 10, -10 < y < 10$. Fig. 5 illustrates the engagement streamline trajectories and engagement capacity characterization for a random convex Gaussian peak surface (Fig. 5A) and a random concave Gaussian valley surface (Fig. 5D).

As shown in Fig. 5A, on the random convex Gaussian peak surface, the ideal trajectory advances along a fixed $y = 0$, climbing over asperities it encounters. In contrast, the streamline trajectory navigates around the asperities, like a winding river flowing around mountains. The figure visually demonstrates the presence of the bypass effect on a random convex Gaussian peak surface and its influence on the engagement streamline. Fig. 5B(I) shows the surface $\kappa$ distribution for the convex random surface composed of random-height Gaussian peaks mentioned above (The color regulation is consistent with that of Fig. 2B.), with colors drawn on a 3D plot. Lower $\kappa$ values are blue, larger values are red, and self-locking points are dark red (consistent with previous sections). Fig. 5B(II) presents the $\kappa$ distributions for the streamline and ideal trajectories on the same surface. The figure shows that the ideal trajectory exhibits larger $\kappa$ peaks, indicating its ability to enter regions with larger $\kappa$ values. In contrast, the $\kappa$ of the streamline trajectory fluctuates within a smaller range, suggesting that the presence of the bypass effect makes it difficult for the streamline trajectory to enter a highly efficient engagement region on a convex random rough surface. Fig. 5B(III) displays a scatter plot of the maximum $\kappa$ distribution for the streamline and ideal trajectories obtained from 100 simulations on the random convex rough surface. The maximum $\kappa$ values for streamline trajectories are marked with blue dots, while those for ideal trajectories are marked with gray dots. The scatter plot shows that the values for ideal trajectories are larger than those for streamline trajectories, which is consistent with the previous analysis. Calculations reveal that the median of the maximum $\kappa$ values for the ideal trajectories was 3.18, while for the streamline trajectories it was 2.87, indicating that the presence of the bypass effect reduced the median of the maximum $\kappa$ by 9.7%.

As can be seen from Fig. 5D, on the random concave Gaussian valley surface, the ideal trajectory advances along a fixed $y = 0$. The streamline trajectory, however, is attracted and trapped when it approaches a rough valley. The figure visually demonstrates the presence of the trap effect on a random concave Gaussian valley surface and its influence on the engagement streamline. Similarly, Fig. 5C(I) shows the surface $\kappa$ distribution for a concave random surface composed of random-height concave Gaussian valleys, with colors plotted on a 3D graph. Fig. 5C(II) presents the $\kappa$ distributions for the streamline and ideal trajectories on this surface. The figure shows that the $\kappa$ of the ideal trajectory fluctuates within a small range, while the streamline trajectory exhibits multiple large fluctuating peaks. This indicates that the trap effect makes it easier for the streamline trajectory to get caught in rough valleys and thus enter a highly efficient self-locking or engagement region. Fig. 5C(III) displays a scatter plot of the maximum $\kappa$ distribution for the streamline and ideal trajectories from 100 simulations on the random concave rough surface. The maximum $\kappa$ values for streamline trajectories are marked with red dots, while those for ideal trajectories are marked with gray dots. The scatter plot shows that the values for ideal trajectories are smaller than those for streamline trajectories, consistent with the previous analysis. The calculated median of the maximum $\kappa$ values was 3.22 for the ideal trajectories and 11.34 for the streamline trajectories, indicating that the presence of the trap effect significantly increased the median of the maximum $\kappa$ for streamline trajectories by 252.2%.

In conclusion, for a complex rough surface composed of multiple ($N = 100$) random Gaussian peaks, the results of the streamline trajectory analysis remain consistent with the previous findings. The bypass effect caused a slight decrease in engagement performance (9.7%) on the random convex Gaussian surface, whereas the trap effect caused a significant increase in engagement performance (252.2%) on the random concave Gaussian surface. This further suggests that for a real rough surface, the concave regions may be the primary load-bearing areas for engagement.

Additionally, it is worth noting that for both the convex and concave random surfaces, the median of the maximum $\kappa$ values for the ideal trajectories showed only a small difference—3.18 for the convex surface and 3.22 for the concave surface, a mere 1.2% difference. This further demonstrates that from a purely static $\kappa$ analysis, there is theoretically no difference between convex and concave surfaces; the real difference in $\kappa$ is brought about by the bypass and trap effects.

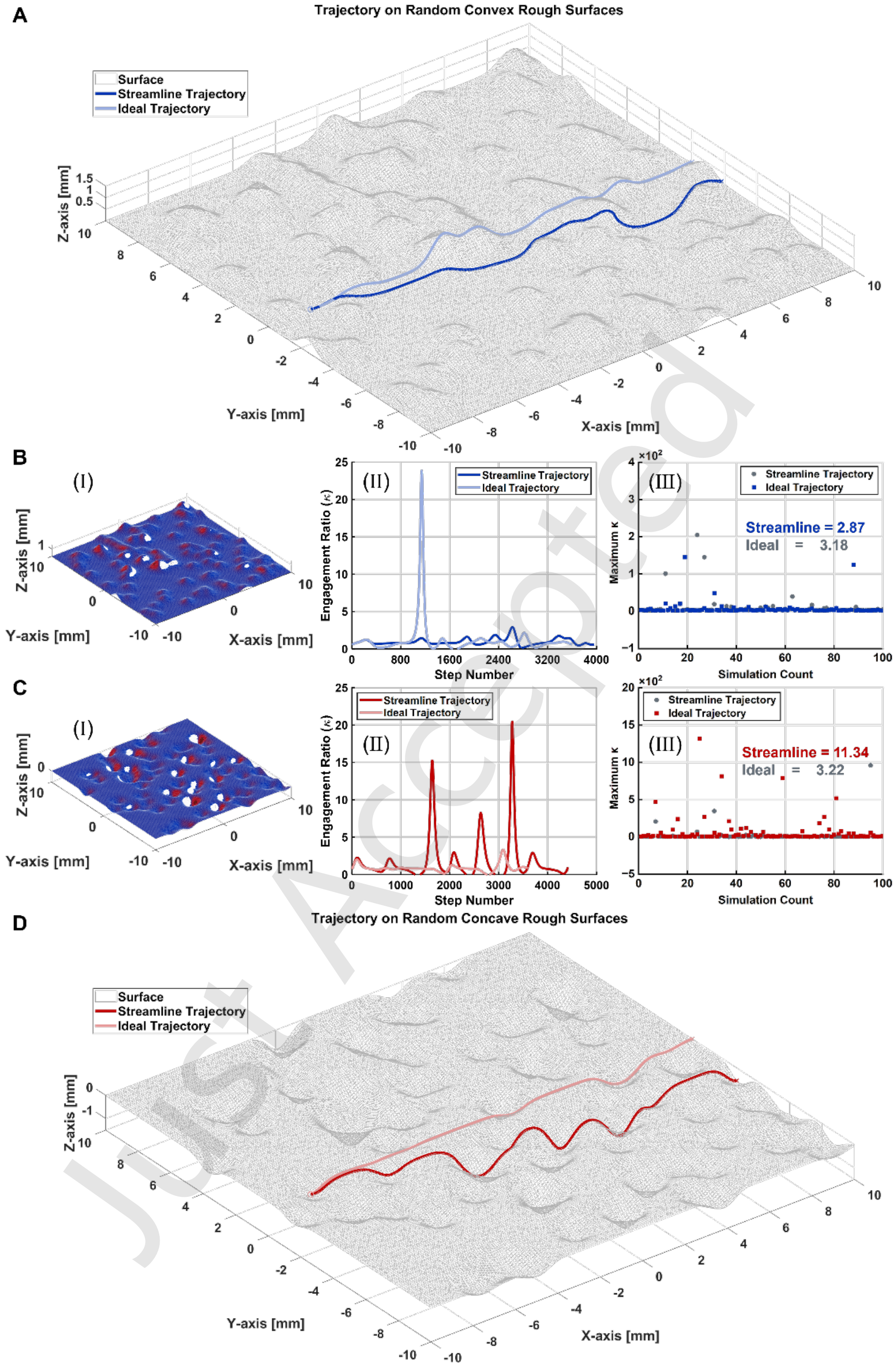


**Fig. 5. Streamline analysis and $\kappa$ distribution on random Gaussian rough surfaces.** (A) Distribution of streamline and ideal trajectories on a random convex Gaussian peak surface. (B) $\kappa$ analysis of engagement streamlines on a random convex Gaussian peak surface. (C) $\kappa$ analysis of engagement streamlines on a random concave Gaussian valley surface. (D) Distribution of streamline and ideal trajectories on a random concave Gaussian valley surface.

### 3.3 Experimental results on sandpapers

To further validate the streamline theory, three different grit sandpapers—P36, P60, and P600—were chosen as experimental materials. This selection was carefully designed to validate the theory across different relative scale ratios between the average particle size ($D_{\mathrm{particle}}$) and the spine tip radius ($R_{\mathrm{tip}} \approx 25$ μm). Specifically, P36 ($D_{\mathrm{particle}} \approx 538$ μm) represents a macro-rough regime ($D_{\mathrm{particle}} \gg R_{\mathrm{tip}}$), analogous to natural tree bark or rough concrete, serving to validate the existence of the predicted bypass and trap effects where geometric interlocking is dominant. P60 ($D_{\mathrm{particle}} \approx 269$ μm) represents a transitional rough regime, bridging the gap between macro-interlocking and micro-friction. Finally, P600 ($D_{\mathrm{particle}} \approx 25.8$ μm) represents a micro-rough regime where the particle size is comparable to the tip radius ($D_{\mathrm{particle}} \approx R_{\mathrm{tip}}$), serving as a boundary condition. In this regime, the finite tip radius acts as a geometric low-pass filter, preventing the spine from entering small valleys. This helps to confirm experimentally that the streamline effects are significant only when the relative scale condition $R_{\mathrm{tip}} \ll R_{\mathrm{surf}}$ is satisfied.

The engagement force data from ten reciprocating movements were measured using a custom-built spine reciprocating force measurement device. Concurrently, a camera placed on the side recorded 8k, 30 fps macro videos. The collected video was analyzed frame by frame with a MATLAB visual recognition code to determine the spine tip's position, and the trajectory of the spine's movement on the sandpaper surface was plotted point by point.

The experimentally measured trajectories and corresponding engagement force data are shown in Fig. 6. Fig. 6A presents three experimental trajectories and the engagement force curves for the spine's movement on the P36 sandpaper surface. The streamline engagement phenomenon of the spine's motion is very apparent in the figure. Due to the presence of the bypass effect, the spine tip's trajectory between the asperities resembles a winding river, seldom climbing over the asperities. A large region of bypass trajectories exists in the middle of the movement, which is reflected in the engagement force curve as a large area of relatively small engagement force (shown in the blue section of the figure). Simultaneously, some concave regions are present in the movement trajectory, where the spine exhibits a clear process of being trapped and then disengaging from the valleys (the trap effect). This is characterized in the streamline trajectory by a significantly greater distance between two consecutive trajectory points compared to others, and in the engagement force curve by a notable peak in the engagement force (indicated by the red arrows in the figure).

Fig. 6B shows three experimental trajectories and the engagement force curves for the spine's movement on the P60 sandpaper surface. A clear streamline engagement phenomenon and a large area of the bypass effect are also visible. Different from the experimental results on P36 sandpaper, the number of valleys exhibiting the trap effect is greater on the P60 sandpaper, which is reflected in more numerous and denser engagement force peaks. However, the height of each peak is smaller. This indicates that, compared to the P36 sandpaper, the trap peaks and valleys on the P60 sandpaper surface are denser but shallower, which is consistent with the definition of sandpaper particle density and grit size.

Fig. 6C shows three experimental trajectories and the engagement force curves for the spine's movement on the P600 sandpaper surface. Unlike the P36 and P60 sandpaper, the experimental results for the P600 sandpaper surface did not show an obvious streamline engagement phenomenon. The trajectories were essentially straight lines following the direction of the motor drive. The engagement force curve was also relatively stable, with no appearance of extremely large force peaks. This suggests that when the particles on a rough surface are fine and dense to a certain extent, and the surface roughness Ra is very small, the streamline engagement effect is not significant, and the spine engagement transforms into a stable friction process.

In summary, the experiments confirm the theoretically analyzed streamline engagement phenomenon and the bypass and trap effects. The presence of the bypass effect leads to regions of smaller values on the engagement force curve, while the presence of the trap effect results in significant localized peaks on the engagement force curve. Furthermore, the prominence of the streamline engagement phenomenon is highly correlated with surface roughness; for surfaces with very low roughness, spine engagement transitions into a stable friction process.

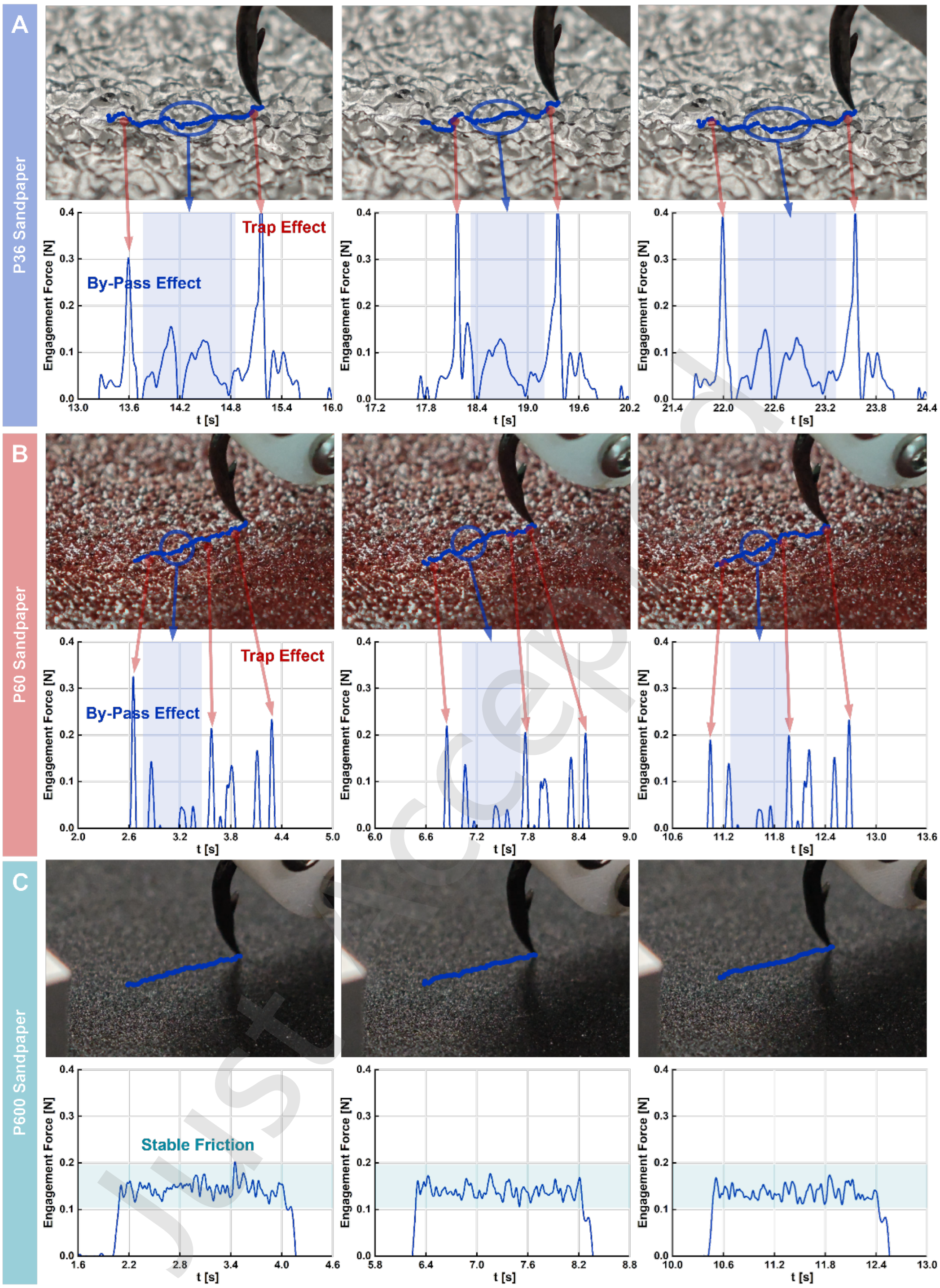


**Fig. 6. Experimental results of engagement streamlines.** (A) Trajectories of engagement streamlines from repeated experiments on P36 sandpaper and the corresponding engagement force curves. (B) Trajectories of engagement streamlines from repeated experiments on P60 sandpaper and the corresponding engagement force curves. (C) Trajectories of engagement streamlines from repeated experiments on P600 sandpaper and the corresponding engagement force curves.

## 3.4 Fractal surface modeling and concavity/convexity analysis

### 3.4.1 Fractal surface generation

The following sections of this paper conduct a further study of the bypass and trap effects based on fractal surfaces. The reasons for choosing fractal surfaces are as follows: (1) Fractal surfaces conform more closely to natural surface morphologies compared to surfaces randomly stacked with a finite number of Gaussian peaks. (2) Fractal surfaces are scale-independent, and their self-similarity indicates that their engagement characteristics do not vary with scale. This also makes them independent of factors such as the spine tip radius, allowing for a focused study of the surface's engagement properties. (3) The concavity and convexity of fractal surfaces are uniform, without a bias towards either concave or convex features, which is crucial for studying engagement effects.

The generation of fractal surfaces is based on a fractional Brownian motion (fBm) model, characterized by a power spectral density (PSD) that follows a power-law decay:

$$P(f) \propto \frac{1}{|f|^{2H+2}} \tag{5}$$

where $f$ is the spatial frequency and $H$ is the Hurst index, which controls the surface roughness.

To generate the surface topography $Z(x,y)$, we employ the spectral synthesis method. An independent complex Gaussian noise field is first constructed in the frequency domain and then filtered by an amplitude response $A(f) = \sqrt{P(f)}$. Finally, the spatial domain surface is obtained via an Inverse Fast Fourier Transform (IFFT) of the filtered spectrum. Fig. 7C shows a schematic of the generated random fractal surface. The engagement streamline analysis, as described previously, was then performed on this surface, yielding the engagement streamline trajectory and the ideal trajectory for a given initial coordinate (Fig. 7D).

Fig. 7E illustrates the control of random fractal surface undulations by the Hurst index $H$. When $H$ is small, low-frequency characteristics are suppressed, and high-frequency characteristics are prominent. The surface appears almost flat without significant waviness, though with more high-frequency details. Consequently, the overall roughness is small, and the surface appears relatively smooth. For example, the $\kappa$ analysis results for fractal surfaces with $H = 0.1$ to 0.3 showed almost no self-locking regions, and only at $H = 0.5$ did sporadic high- $\kappa$ engagement and self-locking regions appear. When $H$ was further increased, the proportion of low-frequency components grew, and the surface waviness increased, presenting larger-scale undulations. The $\kappa$ analysis results showed that as $H$ increases, the area of high- $\kappa$ engagement and self-locking regions significantly expands, with the self-locking region occupying a large portion of the surface when $H = 0.9$. The analysis of the fractal surface morphology for different Hurst indices is consistent with the analysis of the frequency modulation function based on different Hurst indices shown in Fig. 7B.

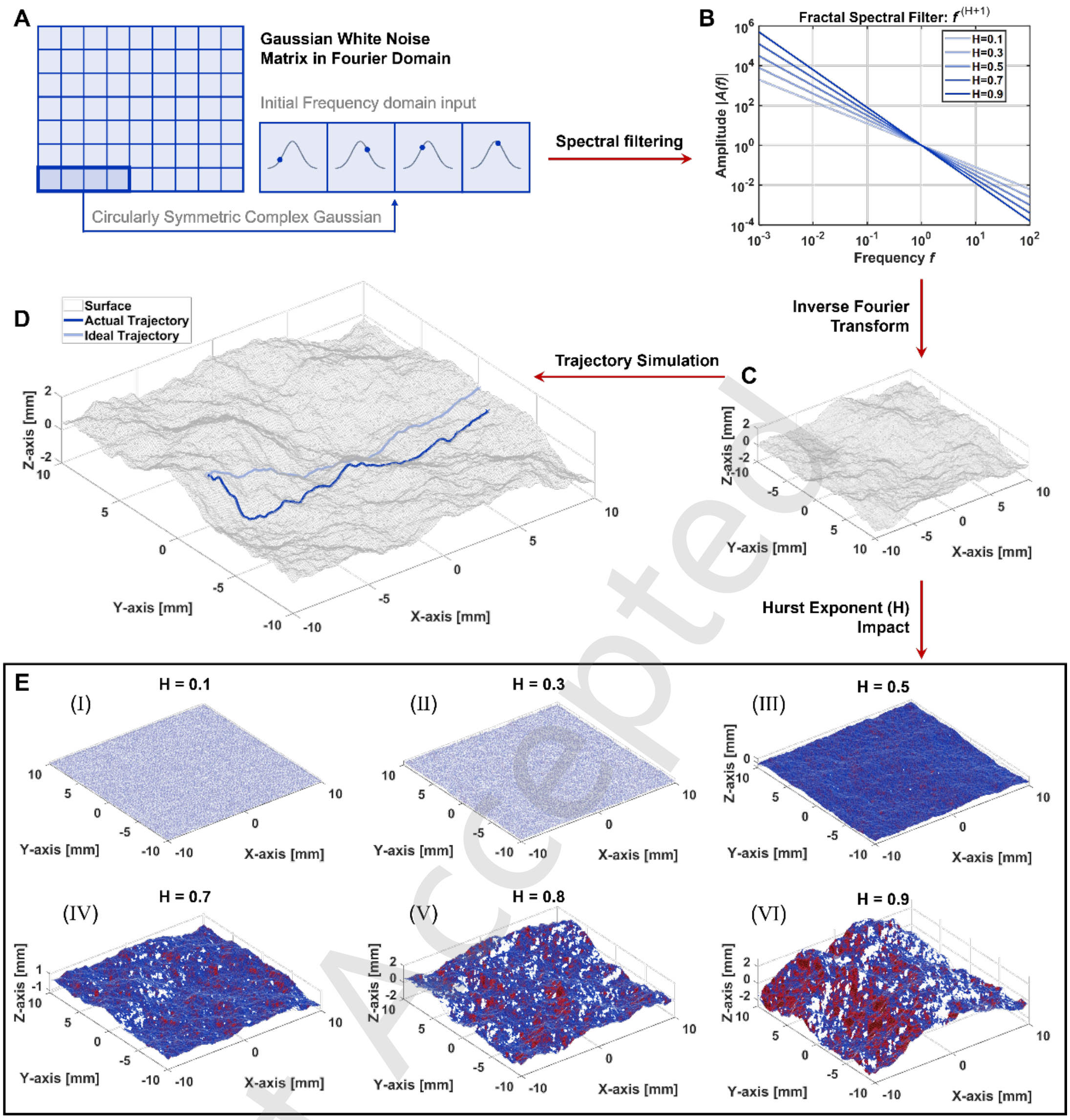


**Fig. 7. Fractal surface generation process and the influence of the Hurst index.** (A) Schematic diagram for the construction of an independent complex Gaussian noise field. (B) Relationship between filter amplitude, Hurst index $H$, and frequency $f$. (C) Diagram of the generated random fractal surface. (D) Streamline and ideal engagement streamline trajectories on a random fractal surface. (E) Control of random fractal surface undulations by the Hurst index $H$.

### 3.4.2 Sectional method for self-locking point concavity/convexity

The bypass and trap effects are related to the concavity and convexity of the surface. For a random Gaussian peak surface, concavity and convexity can be judged from whether the Gaussian peak is convex or concave. However, for a fractal surface, the criteria for judging surface concavity and convexity are more complex.

In this study, a sectional method is used to determine the concavity and convexity of a self-locking point on a fractal surface. Fig. 8 illustrates the morphological characteristics of convex self-locking points (Fig. 8A-B) and concave self-locking points (Fig. 8D-E) on a random fractal surface. The specific calculation method of the sectional method is as follows: assuming the object moves in the x-direction and taking y as a parameter, the sectional line of the surface $z = f(x, y)$ in the x-direction (the $xoy$ plane section) is expressed as $x = g(y)$. According to the implicit function theorem (assuming $\partial f / \partial x \neq 0$), the concavity of the trajectory projected onto the $xoy$ plane is determined by the second-order derivative $\frac{\mathrm{d}^2 x}{\mathrm{d}y^2}$. By differentiating the implicit relationship, we derive:

$$\frac{\mathrm{d}^2 x}{\mathrm{d}y^2} = -\frac{f_{xx} f_y^2 - 2 f_{xy} f_x f_y + f_{yy} f_x^2}{f_x^3} \tag{6}$$

The judgment logic is as follows: A convex self-lock is identified when $\frac{\mathrm{d}^2 x}{\mathrm{d}y^2} > 0$. The geometric meaning of this is that the trajectory forms an upward-opening parabola in the x-direction. When an external driving force $F$ is applied in the positive x-direction at this point, the engagement point tends to disengage backward and toward both sides (as shown in Fig. 8B-C). This manifests the bypass effect mentioned earlier; friction engagement at a convex self-locking point is often unstable and difficult to achieve. The criterion for a concave self-lock is $\frac{\mathrm{d}^2 x}{\mathrm{d}y^2} < 0$. The geometric meaning of this is that the trajectory forms a downward-opening parabola in the x-direction. When an external driving force $F$ is applied in the positive x-direction at this point, the engagement point will converge to a more stable location, eventually reaching a local minimum (as shown in Fig. 8E-F). This manifests the trap effect mentioned earlier; friction engagement at a concave self-locking point is typically stable, which means it can not only bear a larger engagement force and has better anti-interference capability, but also is easier to reach.

Fig. 8 also shows sectional lines in the $yoz$ plane and $xoz$ plane. The morphology of these two sectional lines cannot be used as a criterion for judging the concavity and convexity, but they can provide more information about the stability of the engagement point. For example, the $yoz$-plane section provides lateral information in the y-direction, which can be used to determine whether the engagement self-locking point will slip to the y-sides. The $xoz$-plane section provides topographical information in the x-direction, which can be used to determine whether the subsequent movement is an ascent or a descent, and whether it is prone to vertical slipping.

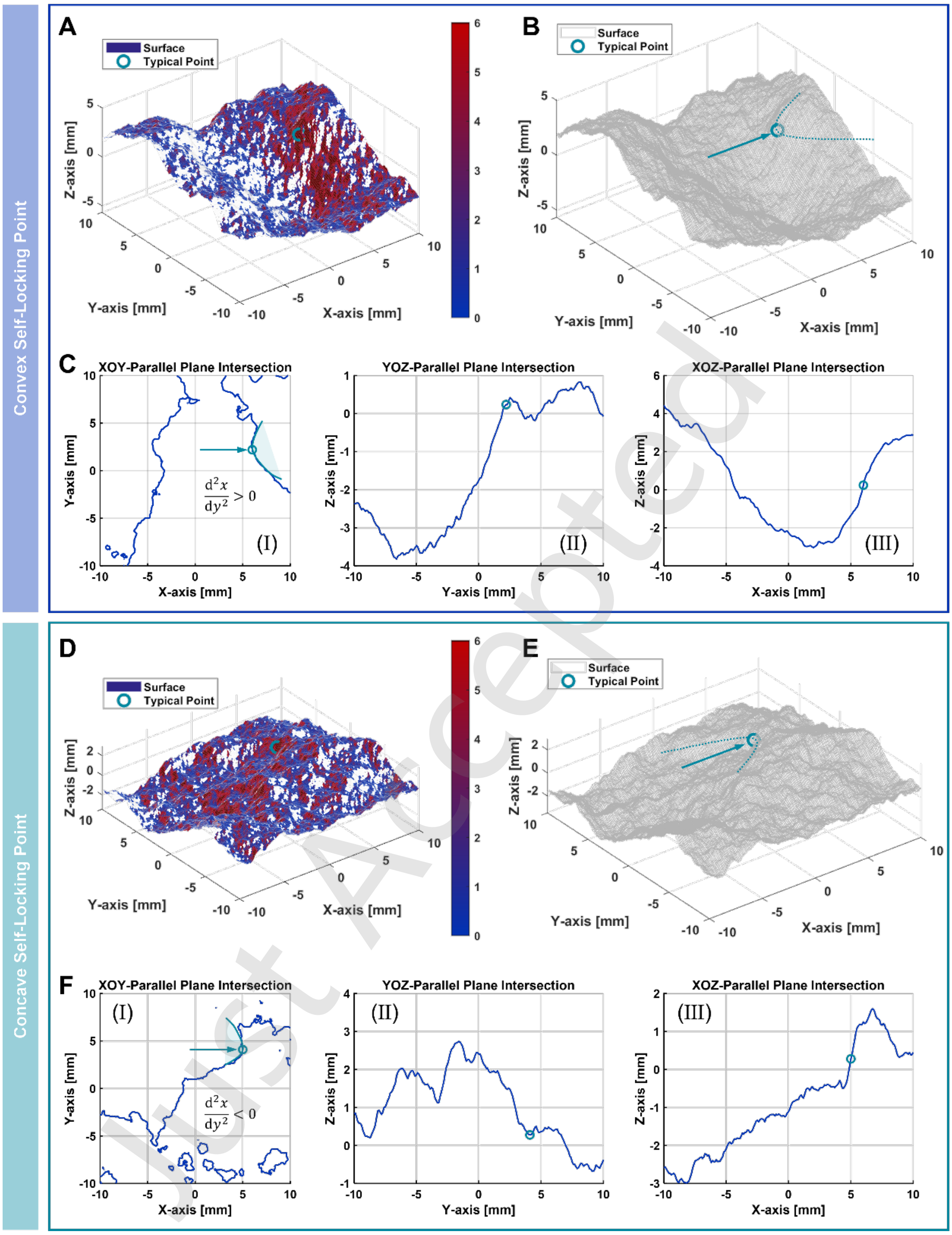



**Fig. 8. Sectional method for determining the concavity and convexity of self-locking points on a fractal surface.** (A) $\kappa$ distribution on the fractal surface with a convex self-locking point. (B) Diagram of the external force direction and sectional concavity/convexity at a convex self-locking point. (C) Calculated sectional curves in the $xoy$, $yoz$, and $xoz$ planes for a convex self-locking point. (D) $\kappa$ distribution on the fractal surface with a concave self-locking point. (E) Diagram of the external force direction and sectional concavity/convexity at a concave self-locking point. (F) Calculated sectional curves in the $xoy$, $yoz$, and $xoz$ planes for a concave self-locking point.

### 3.4.3 Comparison of sectional method and Hessian matrix method

Fig. 9 shows the distinctions and connections between the sectional method and the Hessian matrix method for judging concavity and convexity. Fig. 9A presents the criteria for both methods in a flowchart. The detailed calculation method and criteria for the sectional method were described previously. The Hessian matrix method, on the other hand, is a common approach for analyzing local curvature properties through a surface's second-order partial derivative matrix. The Hessian matrix is defined as:

$$H_s = \begin{bmatrix} \dfrac{\partial^2 f}{\partial x^2} & \dfrac{\partial^2 f}{\partial x \partial y} \\ \dfrac{\partial^2 f}{\partial x \partial y} & \dfrac{\partial^2 f}{\partial y^2} \end{bmatrix} = \begin{bmatrix} f_{xx} & f_{xy} \\ f_{yx} & f_{yy} \end{bmatrix} \tag{7}$$

Concavity and convexity are judged by the determinant of the Hessian matrix. The criterion for a saddle self-locking point is:

$$\det H_s = \frac{\partial^2 f}{\partial x^2}\frac{\partial^2 f}{\partial y^2} - \left(\frac{\partial^2 f}{\partial x \partial y}\right)^2 < 0 \tag{8}$$

Its geometric meaning is that the surface is convex in one direction and concave in another at that point (like a saddle), thus lacking a uniform concavity or convexity. The criterion for a Hessian concave self-lock is:

$$\det H_s > 0 \wedge \frac{\partial^2 f}{\partial x^2} > 0 \tag{9}$$

Its geometric meaning is that the surface is convex downward at this point (like the bottom of a basin). The criterion for a Hessian convex self-lock is:

$$\det H_s > 0 \wedge \frac{\partial^2 f}{\partial x^2} < 0 \tag{10}$$

Its geometric meaning is that the surface is convex upward at this point (like the top of a hill).

It should be noted that a relationship exists between the sectional method and the Hessian matrix method:

$$\frac{\mathrm{d}^2 x}{\mathrm{d}y^2} = -\frac{[f_y \quad -f_x] H_s \begin{bmatrix} f_y \\ -f_x \end{bmatrix}}{f_x^3} = -\frac{v^T H v}{f_x^3}, \qquad H_s = \begin{bmatrix} f_{xx} & f_{xy} \\ f_{yx} & f_{yy} \end{bmatrix} \tag{11}$$

This indicates that the numerator of the sectional method's criterion is actually a quadratic form of the Hessian matrix, specifically, the projected curvature of the Hessian matrix $H$ in the direction of $v = [f_y \quad -f_x]$. Since the research object is a self-locking point, the preset condition for a self-locking point is that the force $F$ points into the surface. Therefore, it can be derived that the denominator of the sectional method: $f_x > 0$. This leads to the following conclusions: (1) If the Hessian matrix is positive definite, then $\det H_s > 0 \wedge \frac{\partial^2 f}{\partial x^2} > 0$. The Hessian criterion is a Hessian concave self-lock, and it can also be derived that $\frac{\mathrm{d}^2x}{\mathrm{d}y^2} < 0$, which means the sectional method must also be a concave self-lock. (2) If the Hessian matrix is negative definite, similarly, the Hessian criterion is a Hessian convex self-lock, and the sectional method must also be a convex self-lock. (3) If the Hessian matrix is indefinite, the relationship between the Hessian criterion and the sectional criterion cannot be determined.

Fig. 9B presents the results of the self-locking point concavity and convexity analysis using the sectional method for fractal surfaces with different Hurst indices. For each Hurst index, 300 random fractal surfaces were generated for simulation, divided into three groups of 100, and the average and standard deviation of the results were calculated. The figure shows that as Hurst index $H$ increases from 0.65 to 0.95, the simulation trajectory's self-locking rate rises from close to 0 to nearly 100%. This indicates that as the Hurst index increases, it becomes easier for the surface engagement streamline to reach a self-locking state, which is consistent with the analysis of the Hurst index's influence in Fig. 7. In the self-locking point concavity and convexity analysis, the proportion of concave self-locks rose rapidly from an initial 70% and stabilized at around 90% after $H = 0.7$. The initially lower concave rate may not be truly representative, as the standard deviation for $H = 0.65$ is very large. This is because the rough surface is still relatively smooth at this point, the self-locking rate is low, and the sample size is insufficient. It is reasonable to assume that the true concave rate may not have a significant relationship with the Hurst index and remains consistently around 90%. Correspondingly, the convex rate decreased from an initial 30% to stabilize at around 10%.

Fig. 9C presents the results of the self-locking point concavity and convexity analysis using the Hessian matrix method for fractal surfaces with different Hurst indices. The self-locking rate curve is not plotted here, as it is consistent with the curve in Fig. 9B. The figure plots the change trends for the three results under the Hessian matrix criteria: the fluctuation is very large between $H = 0.65$ and $H = 0.7$ due to a small amount of data. Subsequently, the proportion of Saddle self-locks stabilized at 30% and gradually decreased to 20%, the proportion of Hessian concave self-locks rose from 70% to 80%, while the proportion of Hessian convex self-locks remained close to 0. This suggests that the Hessian matrix method is more stringent in its judgment of convexity. Furthermore, the proportion of concave self-locks remains significantly higher than that of saddle points. Among all types of self-locking points, the vast majority are still of the Hessian concave type.

In summary, the results from both the sectional method and the Hessian matrix analysis show that concave self-locking points account for the vast majority of self-locking points on random fractal surfaces. As stated earlier, the concavity and convexity of a fractal surface are uniform, without a bias towards either concave or convex features. However, the results of the Monte Carlo simulations reveal that for both the sectional and Hessian matrix methods, the proportion of concave self-locks significantly outweighs that of convex self-locks. This fully demonstrates that under the combined action of the bypass and trap effects, the friction self-locking engagement phenomenon of a spine on a rough surface is predominantly governed by concave points.

Therefore, concave surfaces have a significant inherent advantage over convex rough surfaces for spine engagement.

It is also worth noting that the "bypass" and "trap" effects described herein are governed by geometric interlocking and kinematic constraints, which are inherently scale-independent mechanics. Unlike scale-dependent forces such as van der Waals forces, the findings of this study can theoretically extend to meso- and macro-scale applications. For instance, the interaction between the feet of legged robots and rocky terrain follows similar principles. The critical factor is the relative scale ratio between the engaging tip and the surface asperities. Provided that the engaging tip is sufficiently smaller than the surface features ($R_{\mathrm{tip}} \ll R_{\mathrm{surf}}$), macroscopic grippers or robot feet will exhibit similar streamline dynamics, preferentially settling into concave valleys while bypassing convex asperities, thereby following the same statistical laws of engagement derived in this study.



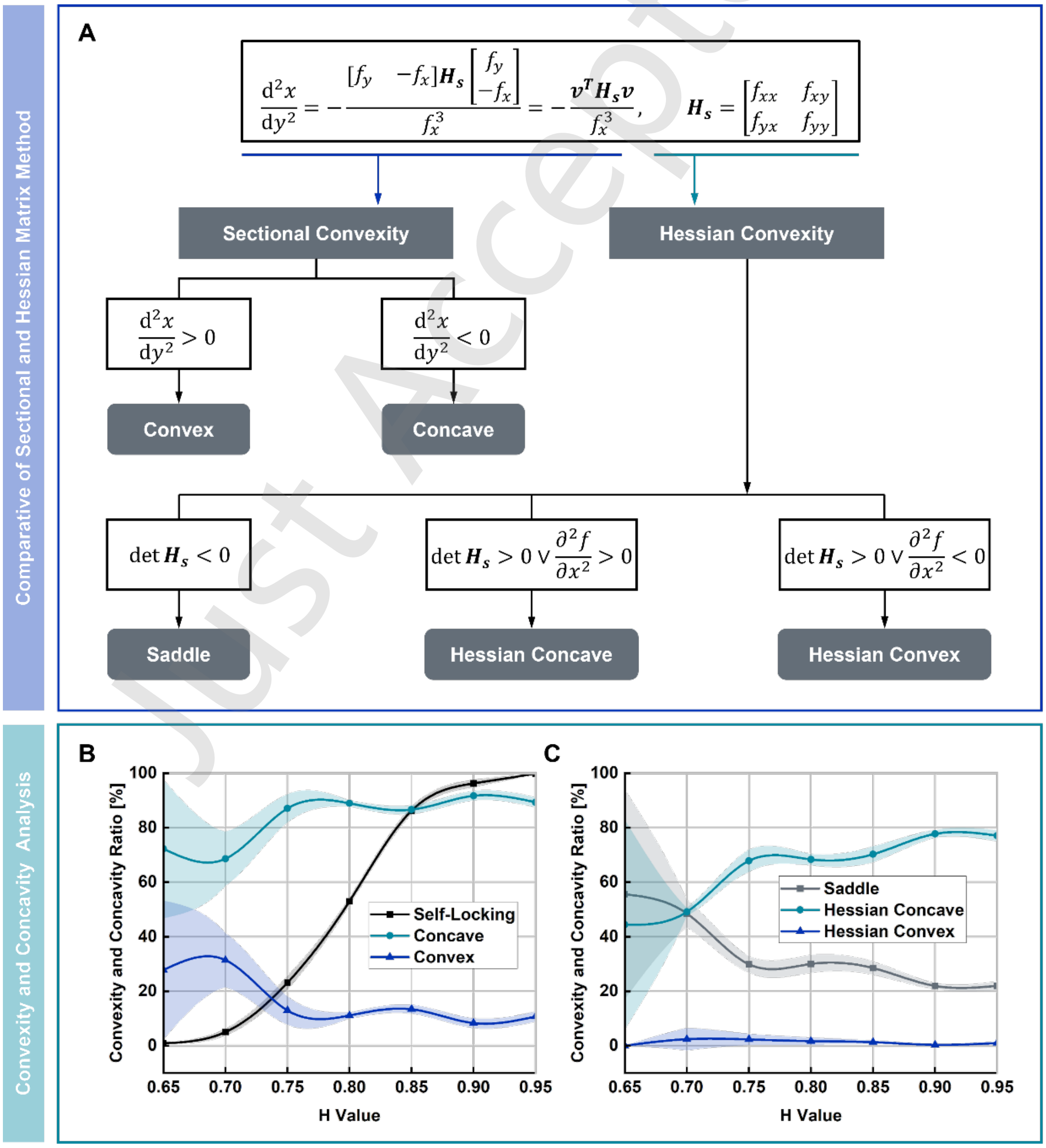


**Fig. 9. Determination of concavity and convexity based on the sectional method and Hessian**

**matrix method.** (A) Flowchart for the determination of concavity and convexity based on the sectional method and Hessian matrix method. (B) Self-locking rate and proportion of concavity/convexity as determined by the sectional method. (C) Proportion of concavity/convexity as determined by the Hessian matrix method.

### 3.5 Design implications for practical grippers

These results suggest several practical design principles for spine-based grippers and rough-terrain robotic feet. First, the effective spine tip radius should remain smaller than the characteristic asperity or valley scale so that concave valleys are mechanically accessible. Second, functional surfaces or contact strategies that expose valley-like or groove-like features should be preferred because they enlarge the capture region for stable self-locking. Third, the engagement speed should be controlled so that the dimensionless engagement inertia number remains in the quasistatic regime. Finally, multi-spine arrays with staggered spatial layouts may increase the probability that at least one spine samples a favorable concave region, thereby improving robustness for practical robot attachment.

## 4. Limitations and future work

While the proposed streamline theory effectively illustrates the micro-engagement mechanisms, certain limitations in the current modeling approach should be acknowledged. First, the point contact assumption simplifies the geometric interaction. The tip radius adopted in the present experiments, $R_{\mathrm{tip}} \approx 25\ \mu\mathrm{m}$, corresponds to a stabilized worn state after 50 concave-valley capture-release cycles, and therefore provides a representative radius for the repeated engagement tests rather than an ideal pristine tip. Nevertheless, a finite or further worn tip radius in practical applications would effectively smooth the surface roughness, acting as a geometric low-pass filter. This filtering mainly suppresses the influence of surface undulations whose length scale is comparable to or smaller than the current tip radius, thereby reducing access to small concave valleys, lowering peak engagement forces, and potentially diminishing the quantitative gain of the trap effect. For macroscopically rough surfaces with millimeter-scale features, however, this tip-scale filtering does not eliminate the larger-scale streamline phenomenon, and bypass/trap behavior can still be clearly observed. The P600 boundary case provides indirect support for this scale effect because the streamline phenomenon becomes weak when the surface feature size approaches the tip radius. Second, the quasi-static assumption neglects inertial dynamics. In high-speed scenarios, stick-slip phenomena and inertial jumping may occur. Specifically, high tangential velocities could cause the spine to skip over narrower concave traps, thereby reducing the quantitative capture efficiency of the trap effect compared to the quasi-static prediction (e.g., the calculated 252.2% gain might diminish). Additionally, possible quantitative discrepancies in peak forces may arise from the resolution limits of surface metrology in deep valleys and local material wear, which are not captured in the rigid-body simulation. Third, the present model analyzes a single spine, whereas practical robotic grippers typically employ coupled spine arrays. In such arrays, the bypass-induced diversion of one spine may be offset by neighboring spines through spatial coupling, compliant load sharing, and staggered sampling of adjacent surface features. When the spacing between neighboring spines is comparable to the capture width of concave valleys, array-level compression and redistribution may increase the probability of at least one spine entering a favorable trap. Nevertheless, quantitative prediction of these collective effects requires a future multi-contact model. Despite these limitations, the fundamental qualitative mechanism, where geometric interlocking favors concave topographies while convex asperities induce instability, remains valid. Future work will focus on incorporating dynamic inertial effects, measuring further tip evolution during longer repeated engagement, and extending the single-spine analysis to multi-spine arrays.

## 5. Conclusion

This study proposes a streamline trajectory analysis method, providing a new theoretical framework for understanding the micro-dynamic behavior of bio-inspired spines engaging with complex rough surfaces. Through this method, two previously unreported engagement phenomena, the "bypass effect" and the "trap effect," were revealed and systematically investigated for the first time. This discovery challenges the traditional understanding of predicting engagement performance based solely on the static geometric parameters of a rough surface.

The research findings indicate that the "bypass effect" causes a spine's trajectory to actively deviate from high-engagement-ratio regions when encountering convex asperities, thereby reducing engagement effectiveness. Conversely, the "trap effect" causes the spine's trajectory to converge and become trapped in valleys, which significantly enhances the engagement load-bearing capacity. Through large-scale numerical simulations on idealized single-peak Gaussian surfaces, randomly distributed Gaussian surfaces, and fractal surfaces that more closely resemble real morphologies, the significant differences between these two effects were successfully quantified: the enhancing effect of the trap effect on engagement performance far outweighs the negative impact of the bypass effect. Experimental validation further confirms the existence of the streamline phenomenon and visually characterizes the bypass and trap effects in practice through engagement force curves on P36, P60, and P600 sandpapers, proving the correctness of the theoretical analysis.

More importantly, an analysis of the concavity and convexity of self-locking points was conducted using a combination of the sectional method and the Hessian matrix method. This analysis found that even though the concavity and convexity of fractal surfaces are uniformly distributed, almost all stable self-locking engagements occur in concave regions. This finding establishes the dominant role of valleys in achieving efficient friction self-locking.

The results provide a theoretical foundation for the development of a new generation of bio-inspired grippers with superior adhesive performance and predictable engagement behavior. In practical applications, this framework can guide the selection of spine-tip radius, contact velocity, target surface morphology, and multi-spine array spacing for rough-wall climbing, terrain anchoring, micromanipulation, and aerospace exploration.

**Acknowledgements**

The authors are grateful for the financial support of the National Natural Science Foundation of China (Grant No. 52175176 and No.52405202).

**Reference**


[1] Bußhardt P, Kunze D, Gorb SN. Interlocking-based attachment during locomotion in the beetle Pachnoda marginata (Coleoptera, Scarabaeidae). Sci Rep 2014;4:6998. https://doi.org/10.1038/srep06998.

[2] Song Y, Dai Z, Wang Z, Ji A, Gorb SN. The synergy between the insect-inspired claws and adhesive pads increases the attachment ability on various rough surfaces. Sci Rep 2016;6:26219. https://doi.org/10.1038/srep26219.

[3] Ditsche-Kuru P, Barthlott W, Koop JHE. At which surface roughness do claws cling? Investigations with larvae of the running water mayfly Epeorus assimilis (Heptageniidae, Ephemeroptera). Zoology 2012;115:379–88. https://doi.org/10.1016/j.zool.2011.11.003.

[4] Pope MT, Kimes CW, Jiang H, Hawkes EW, Estrada MA, Kerst CF, et al. A Multimodal Robot for Perching and Climbing on Vertical Outdoor Surfaces. IEEE Trans Robot 2017;33:38–48. https://doi.org/10.1109/TRO.2016.2623346.

[5] Roderick WRT, Cutkosky MR, Lentink D. Bird-inspired dynamic grasping and perching in arboreal environments. Sci Robot 2021;6:eabj7562. https://doi.org/10.1126/scirobotics.abj7562.

[6] Zi P, Xu K, Tian Y, Ding X. A mechanical adhesive gripper inspired by beetle claw for a rock climbing robot. Mechanism and Machine Theory 2023;181:105168. https://doi.org/10.1016/j.mechmachtheory.2022.105168.

[7] Li M, Su M, Xie R, Zhang Y, Zhu H, Zhang T, et al. Development of a Bio-inspired Soft Gripper with Claws n.d.

[8] Dai Z, Gorb SN, Schwarz U. Roughness-dependent friction force of the tarsal claw system in the beetle Pachnoda marginata (Coleoptera, Scarabaeidae) n.d.

[9] Li X, Chen W, Li X, Hou X, Zhao Q, Meng Y, et al. An Underactuated Adaptive Microspines Gripper for Rough Wall. Biomimetics 2023;8:39. https://doi.org/10.3390/biomimetics8010039.

[10] Liu Y, Wang L, Niu F, Li P, Li Y, Mei T. A Track-type Inverted Climbing Robot with Bio-inspired Spiny Grippers. J Bionic Eng 2020;17:920–31. https://doi.org/10.1007/s42235-020-0093-5.

[11] Liu Y, Huang X, Pan H, Li S, Li P. Design of a Spiny Foot with Fluid-filled Sacs for Climbing Robots. 2021 IEEE International Conference on Real-time Computing and Robotics (RCAR), Xining, China: IEEE; 2021, p. 336–40. https://doi.org/10.1109/RCAR52367.2021.9517486.

[12] Wang S, Jiang H, Cutkosky MR. A palm for a rock climbing robot based on dense arrays of micro-spines. 2016 IEEE/RSJ International Conference on Intelligent Robots and Systems (IROS), Daejeon, South Korea: IEEE; 2016, p. 52–9. https://doi.org/10.1109/IROS.2016.7759034.

[13] Ruotolo W, Roig FS, Cutkosky MR. Load-Sharing in Soft and Spiny Paws for a Large Climbing Robot. IEEE Robotics and Automation Letters 2019;4:1439–46. https://doi.org/10.1109/LRA.2019.2897002.

[14] Parness A, Frost MA, Thatte N, King JP, Witkoe K, Nevarez M, et al. Gravity-independent Rock-climbing Robot and a Sample Acquisition Tool with Microspine Grippers. Journal of Field Robotics 2013;30.

[15] Liu G, Liu Y, Wang X, Wu X, Mei T. Design and experiment of a bioinspired wall-climbing robot using spiny grippers. 2016 IEEE International Conference on Mechatronics and Automation, 2016, p. 665–70. https://doi.org/10.1109/ICMA.2016.7558642.

[16] Ji A, Zhao Z, Manoonpong P, Wang W, Chen G, Dai Z. A Bio-inspired Climbing Robot with Flexible Pads and Claws. J Bionic Eng 2018;15:368–78. https://doi.org/10.1007/s42235-018-0028-6.

[17] Uno K, Takada N, Okawara T, Haji K, Candalot A, Ribeiro WFR, et al. HubRobo: A Lightweight Multi-Limbed Climbing Robot for Exploration in Challenging Terrain. 2020 IEEE-RAS 20th International Conference on Humanoid Robots (Humanoids), Munich, Germany: IEEE; 2021, p. 209–15. https://doi.org/10.1109/HUMANOIDS47582.2021.9555799.

[18] Nagaoka K, Minote H, Maruya K, Shirai Y, Yoshida K, Hakamada T, et al. Passive Spine Gripper for Free-Climbing Robot in Extreme Terrain. IEEE Robot Autom Lett 2018;3:1765–70. https://doi.org/10.1109/LRA.2018.2794517.

[19] Haynes GC, Khripin A, Lynch G, Amory J, Saunders A, Rizzi AA, et al. Rapid pole climbing with a quadrupedal robot. 2009 IEEE International Conference on Robotics and Automation, Kobe: IEEE; 2009, p. 2767–72. https://doi.org/10.1109/ROBOT.2009.5152830.

[20] Parness A, Abcouwer N, Fuller C, Wiltsie N, Nash J, Kennedy B. LEMUR 3: A limbed climbing robot for extreme terrain mobility in space. 2017 IEEE International Conference on Robotics and Automation (ICRA), 2017, p. 5467–73. https://doi.org/10.1109/ICRA.2017.7989643.

[21] Chen TG, Miller B, Winston C, Schneider S, Bylard A, Pavone M, et al. ReachBot: A Small Robot with Exceptional Reach for Rough Terrain. 2022 International Conference on Robotics and Automation (ICRA), Philadelphia, PA, USA: IEEE; 2022, p. 4517–23. https://doi.org/10.1109/ICRA46639.2022.9811949.

[22] Kim S, Asbeck AT, Cutkosky MR, Provancher WR. SpinybotII: Climbing Hard Walls with Compliant Microspines n.d.

[23] Xu FY, Wang XS, Jiang GP, Gao Q. Initial design and analysis of a rough concrete building-climbing robot based on biomimetic grip claws. 2013 IEEE International Conference on Robotics and Biomimetics (ROBIO), Shenzhen, China: IEEE; 2013, p. 408–13. https://doi.org/10.1109/ROBIO.2013.6739493.

[24] Picardi G, Chellapurath M, Iacoponi S, Stefanni S, Laschi C, Calisti M. Bioinspired underwater legged robot for seabed exploration with low environmental disturbance. Science Robotics 2020;5:eaaz1012. https://doi.org/10.1126/scirobotics.aaz1012.

[25] Zi P, Xu K, Chen J, Wang C, Zhang T, Luo Y, et al. Intelligent Rock-Climbing Robot Capable of Multimodal Locomotion and Hybrid Bioinspired Attachment. Advanced Science 2024;11:2309058. https://doi.org/10.1002/advs.202309058.

[26] Koh J-S, An S-M, Cho K-J. Finger-sized climbing robot using artificial proleg. 2010 3rd IEEE RAS & EMBS International Conference on Biomedical Robotics and Biomechatronics, Tokyo, Japan: IEEE; 2010, p. 610–5. https://doi.org/10.1109/BIOROB.2010.5628000.

[27] Birkmeyer P, Gillies AG, Fearing RS. CLASH: Climbing Vertical Loose Cloth n.d.
[28] Spenko MJ, Haynes GC, Saunders JA, Cutkosky MR, Rizzi AA, Full RJ, et al. Biologically inspired climbing with a hexapedal robot. Journal of Field Robotics 2008;25:223–42. https://doi.org/10.1002/rob.20238.
[29] Wang S, Jiang H, Myung Huh T, Sun D, Ruotolo W, Miller M, et al. SpinyHand: Contact Load Sharing for a Human-Scale Climbing Robot. Journal of Mechanisms and Robotics 2019;11:031009. https://doi.org/10.1115/1.4043023.
[30] Provancher WR, Clark JE, Geisler B, Cutkosky MR. Towards Penetration-based Clawed Climbing. Climbing and Walking Robots, Berlin, Heidelberg: Springer Berlin Heidelberg; 2005, p. 961–70. https://doi.org/10.1007/3-540-29461-9_94.
[31] Jiang H, Han X, Jing Y, Guo N, Wan F, Song C. Rigid–Soft Interactive Design of a Lobster-Inspired Finger Surface for Enhanced Grasping Underwater. Front Robot AI 2021;8:787187. https://doi.org/10.3389/frobt.2021.787187.
[32] Daltorio KA, Wei TE, Gorb SN, Ritzmann RE, Quinn RD. Passive Foot Design and Contact Area Analysis for Climbing Mini-Whegs. Proceedings 2007 IEEE International Conference on Robotics and Automation, Roma: IEEE; 2007, p. 1274–9. https://doi.org/10.1109/ROBOT.2007.363160.
[33] Daltorio KA, Wei TE, Horchler AD, Southard L, Wile GD, Quinn RD, et al. Mini-WhegS™ climbing steep surfaces with insect-inspired attachment mechanisms. The International Journal of Robotics Research 2009;28:285–302. https://doi.org/10.1177/0278364908095334.
[34] Liu Y, Sun S, Wu X, Mei T. A leg-wheel wall-climbing robot utilizing bio-inspired spine feet. 2013 IEEE International Conference on Robotics and Biomimetics (ROBIO), Shenzhen, China: IEEE; 2013, p. 1819–24. https://doi.org/10.1109/ROBIO.2013.6739732.
[35] Parness A. Anchoring foot mechanisms for sampling and mobility in microgravity. 2011 IEEE International Conference on Robotics and Automation, 2011, p. 6596–9. https://doi.org/10.1109/ICRA.2011.5980584.
[36] Parness A, Frost M, Thatte N, King JP. Gravity-independent mobility and drilling on natural rock using microspines. 2012 IEEE International Conference on Robotics and Automation, St Paul, MN, USA: IEEE; 2012, p. 3437–42. https://doi.org/10.1109/ICRA.2012.6224933.
[37] Parness A, Willig A, Berg A, Shekels M, Arutyunov VA, Dandino CM, et al. A microspine tool: Grabbing and anchoring to boulders on the Asteroid Redirect Mission. 2017 IEEE Aerospace Conference 2017:1–10.
[38] Jiang H, Wang S, Cutkosky MR. Stochastic models of compliant spine arrays for rough surface grasping. The International Journal of Robotics Research 2018;37:669–87. https://doi.org/10.1177/0278364918778350.
[39] Wang S, Jiang H, Cutkosky MR. Design and modeling of linearly-constrained compliant spines for human-scale locomotion on rocky surfaces. The International Journal of Robotics Research 2017;36:985–99. https://doi.org/10.1177/0278364917720019.
[40] Asbeck AT, Kim S, McClung A, Parness A, Cutkosky MR. Climbing Walls with Microspines n.d.

[41] Asbeck AT, Kim S, Cutkosky MR, Provancher WR, Lanzetta M. Scaling Hard Vertical Surfaces with Compliant Microspine Arrays. The International Journal of Robotics Research 2006;25:1165–79. https://doi.org/10.1177/0278364906072511.
[42] Asbeck AT, Cutkosky MR. Designing Compliant Spine Mechanisms for Climbing. Journal of Mechanisms and Robotics 2012;4:031007. https://doi.org/10.1115/1.40066591.
[43] Xiang Z, Zhou X, Chen W, Li X, Bai P, Meng Y, et al. Capability and probability of frictional engagement of spines on rough surfaces. Tribology International 2025;204:110533. https://doi.org/10.1016/j.triboint.2025.110533.